AUTOMATIC DETECTION OF MOISTURES IN DIFFERENT CONSTRUCTION MATERIALS FROM THERMOGRAPHIC IMAGES

I. Garrido*[1], S. Lagüela[2], S. Sfarra[3], F.J. Madruga[4] and P. Arias[1]

[1] Applied Geotechnologies Research Group, Mining & Energy Engineering School, University of Vigo, Rúa Maxwell s/n, 36310 Vigo (Spain)

[2] Department of Cartographic and Terrain Engineering, EPS Ávila, University of Salamanca, Calle Hornos Caleros 50, 05003 Ávila (Spain)

[3] Department of Industrial and Information Engineering and Economics (DIIIE), University of L'Aquila, Piazzale E. Pontieri 1, I-67100 Monteluco di Roio, L'Aquila, AQ, Italy

[4] Photonics Engineering Group, CIBER-bbn and IDIVAL, University of Cantabria, Av. De Los Castros s/n 39005 Santander, Cantabria, Spain

***Corresponding author:** ivgarrido@uvigo.es**; (+34) 986813499**

Abstract:

Moisture is a pathology that damages all type of construction materials, from materials of building envelopes to materials of bridges. Its presence can negatively affect the users' conditions of indoor comfort. Furthermore, heating and cooling energy demand can be increased by the presence of moist materials. InfraRed Thermography (IRT) is a common technique in the scientific field to detect moisture areas, because of its non-destructive, non-contact nature. In addition, IRT allows an earlier moisture detection compared to the analysis using visible images. In order to optimize thermographic inspections, this paper presents one of the first methodologies for the automatic detection of moisture areas affecting the surface of construction materials. The methodology is based on the application of visible image processing techniques adapted to thermographic images through the consideration of an image conversion format, a thermal criterion and a thermal and a geometric filter. The *precision*, *recall* and *F-score* parameters obtained are around 83.5%, 73.5% and 72.5%, respectively, considering the false

positives/negatives through a series of 12 tests made in different construction materials and ambient conditions, comparing the preliminary results with existing methodologies.

Keywords: moisture, InfraRed Thermography, automation, adapted visible image processing, construction materials, different environmental conditions.

1. Introduction

Moisture is a pathology that appears in construction materials, such as materials of building envelopes or bridges, for several causes: rain water/melting snow infiltration, condensation, capillary rise of ground water or sewer system overflow. The previous events are mostly caused by natural disasters or human errors, such as flooding and disrepair of the compositions, respectively. In addition, most decay mechanisms that affect construction materials involve the role of water:

(1) biological/mould growth appears due to the presence of water that promotes the development and expansion of the mould in non-nutritive materials with traces of organic matter contamination.

(2) oxidation of metallic materials, as in the reinforcements of the reinforced concrete, is caused by the presence of water.

(3) efflorescence/salt crystallization is due to the change of state of the water present in the material from liquid to vapour, and the subsequent precipitation and crystallization of certain soluble salts in water.

(4) cracking and detachment are the consequence of the change of state of the water present in the material from liquid to vapour or from liquid to solid, changes where the water volume grows as gas or frost and generates pressure inside the pores of the moist materials.

Besides, users' conditions of indoor comfort can be negatively affected because of excess moisture [1-3]. According to World Health Organization (WHO) guidelines *Dampness and Mould* [4], moisture is a problem in 10 to 50% of the buildings in Australia, Europe, India, Japan and North America. On the other hand, fungal growth deteriorates 15 to 40% of North America and

Northern European homes [5]. The symptoms reported by occupants in mouldy buildings are many and diverse, such as allergic respiratory diseases, including asthma and hypersensitivity pneumonitis [6, 7]; and the relationship between fungal exposure and development of type I allergy has been proven [8].

In a more energetic approach, heating and cooling energy demand of a building could be increased by the presence of moist materials, since their thermal conductivities are higher than those in their surroundings [1]. In addition, the presence of moisture inside any insulation material negatively affects its properties because the thermal conductivity of water (in liquid state) is 25 times higher than that of air at room temperature [9], and about 18 times higher than the mean thermal conductivity of the most common building insulation materials [10]. Because the ambient temperature is normally below zero degrees Celsius (ºC) for prolonged periods during winter in northern Europe and America, moisture generates cracks in the construction materials due to frost-defrost cycles, in some cases damaging the insulation material and provoking the appearance of thermal bridges. However, in temperate climatic areas during winter, walls with considerable thickness prevent the frost of the water content inside thanks to a higher value of their thermal inertias, and the damage of frost-defrost cycles is concentrated on the surfaces [11].

In the light of the foregoing, it is necessary to detect moisture areas, both at specific times and over time (monitoring), before visible defects appear. In this way, it is possible to perform preventive maintenance measures, such as the control of the moisture level so as not to exceed the limit at which mould begins to grow or the removal of moisture through condensation in interior materials by means of forced ventilation or dehumidifier. The targets of the prior tasks are: (1) helping to maintain the good health in the construction materials affected, with neither material loss nor human diseases, (2) preserving users' indoor comfort conditions and (3) avoiding excessive energy use for heating/cooling [1, 12, 13].

Non-Destructive Testing (NDT) methods are ideal tools to detect moisture areas because they do not damage the construction materials under study [14]. For example, [15] presents a study of the use of the Terrestrial Laser Scanning (TLS) technique for the detection of moisture in building materials. Among the conclusions reached, they realized that the TLS using an infrared laser beam is significantly more suitable to detect saturation on surfaces with local discolorations (typical in ancient and historical structures) than the use of the TLS based on green or any other visible light.

According to the last paragraph, InfraRed Thermography (IRT) stands among the most appropriate NDT methods for detecting moisture areas in construction materials, since this technique mitigates one of the limitations of the NDTs methods that work within the visible spectrum. This limitation stays in the fact that a moisture area affecting the surface of a construction material is only visible to the human eye if: (1) any algae or plant grows, or (2) a certain visible colour change occurs due to the optical properties of the material surface under the presence of a considerable amount of water. By contrast, this pathology is rapidly detected within the thermal infrared spectrum [16]. Some evaluation tests are performed in the Section 4.3.2. for comparison.

Therefore, there are several IRT studies destined to meet the above objective under different environmental conditions (see Section 2.1). However, all such researches, except [17], require the interpretation of the data by a human operator. Consequently, all these works involve a high-level of subjectivity and mainly rely on the expertise of the operator. For this reason, the automation of the interpretation of the moisture detection is proposed as a solution to minimize the risk of a wrong assessment of the moisture areas. In doing so, the understanding and knowledge of the geometry and of the temperature distribution of this anomaly with regard to its unaltered surroundings is required for the establishment of the conditions necessary for the correct identification of moisture areas [18].

Thus, in a similar manner to [17], where the focus is set on the automatic detection of thermal bridges and moisture areas in different exterior/interior surfaces of building envelopes through the application of IRT, the present paper aims at: (1) developing an automatic methodology for the detection of the contours of moisture areas in construction materials on thermal images, and (2) showing the comparison results with regard to the tests performed in [17]. The proposed methodology will facilitate the IRT inspections and minimize human subjectivity in data interpretation. Furthermore, it will contribute as additional information in multi-technique studies that analyse materials of structures with special interest of conservation. For instance, [19] integrates IRT and the water absorption test by contact sponge allowing to determine the origin of the absorption and the diffusion and evaporation of water that vary the texture of the surface analysed. [20] integrates the reflectography technique and IRT allowing to detect of features such as underdrawings and sketches on paintings.

Regarding the processing of thermal images, the application of visible image processing techniques to detect a specific anomaly in a thermal image is not straightforward, as these techniques are designed for images acquired with RGB cameras or cameras sensitive to the visible spectrum, which present a higher resolution than the cameras used in IRT applications (Thermal InfraRed (TIR) cameras). In other words, thermal images do not have the number of pixels necessary to present valid results using visible image processing techniques [17]. For this reason, instead of using image processing techniques that group pixels of the image under study according to some image characteristic parameter (colour, texture or intensity, among others), such as the region splitting technique [21], IRT works use other different approaches. For instance, there are IRT studies that apply statistical approaches in order to extract and separate different features present in the thermal images under investigation and eliminate most of the existing noise, such as PCT or Nonnegative Matrix Factorization (NMF) [22], or IRT works that simultaneously combine the advantages of the two types of heating process corresponding to active IRT (see Section 2), in order to unscrambled the temperature evolution over the field of view under study by performing the Fourier Transform (FT), known this approach as Pulse Phase Thermography (PPT) [23].

However, to meet the paper objectives, instead of using image processing algorithms developed for thermal images, this work proposes the application of various visible image processing techniques in the thermal images, after some adaptations. These techniques: (1) will increase the difference in the pixel-value between the moisture areas and the unaltered zone of each thermal image (*thresholding* technique) and remove noise while keeping the edges intact (*bilateral filtering* technique) and then, (2) will allow the detection of the contours of moisture areas according to the highest difference of pixel-value in each thermal image (*findContours* technique). Regarding the adaptations, the following actions are performed, in this order: (1) the consideration of a format conversion to the thermal images before the application of the *bilateral filtering* technique (Section 3.2.1.), (2) the introduction of a thermal criterion (Section 3.2.2.) to apply the *thresholding* technique, based on the temperature distribution of the pathology concerning its environment and, finally, (3) the implementation of a geometric and a thermal filter (Section 3.2.3.) for the *findContours* technique application. The corresponding graphical representation is shown in Fig. 1.

Thus, this work is organized as follows: Section 2 briefly describes the InfraRed Thermography concept and its main applications, including a brief review of the most recent IRT works that detect moisture areas affecting the surfaces of different construction materials; Section 3 explains the methodology proposed, including the description of the recommended requirements during the acquisition stage and the theoretical assumptions for the thermal criterion introduced in the *thresholding* technique; Section 4 describes the surfaces of the construction materials selected and their inspections for the evaluation of the methodology and presents the preliminary results, including the comparison with regard to the tests performed in [17]. Last, Section 5 contains the conclusions reached after the evaluation of the preliminary results.

2. InfraRed Thermography theory and main applications

The basis of IRT is to measure the thermal radiation emitted by the surface of an object under study in real time and then obtain the corresponding temperature value after a conversion process. This thermal radiation belongs to the Thermal InfraRed (TIR) band, which is the spectral band located in the wavelength range 7 µm @ 14 µm, within the electromagnetic spectrum [24].

There are mainly two different thermographic acquisition and two different thermographic post-acquisition procedures for analysing construction materials. Regarding acquisition procedures, some IRT studies use an external and artificial mechanism of thermal excitation in the material under study, with the purpose of taking thermal images during the heating or cooling processes. This type of acquisition is known as active IRT [24], used with the objective of producing a higher thermal contrast in the surface analysed to create, for example, a thermal contrast in possible subsurface defects, and make them more visible on the thermal images [25]. The other type of acquisition procedure consists of analysing the natural thermal behaviour of the material through a natural thermal excitation source, such as solar radiation. Thus, in this type of acquisition, known as passive IRT, the analysis is performed under real conditions without artificial thermal excitation. Therefore, the detection of subsurface defects is more limited with regard to the size and depth of the defect.

As for the different post-acquisition procedures, they depend on the type of use performed of the temperature values measured in each IRT research. Some IRT works focus on the temperature distribution or the relative pixel-values of the thermal images, with the purpose of detecting the absence or existence of areas of pathologies rather than classifying the severity and/or calculating the thermophysical properties of the defects detected or of the construction material under study. This type of post-acquisition procedure is known as qualitative IRT, and the precise knowledge of the temperature values is not required. Then, the emissivity, reflected temperature and attenuation coefficient parameters are not taken into account for the correction of the thermal images taken with the TIR camera. Otherwise, the procedure name corresponds to quantitative IRT [24].

Therefore, from an image with the pixels representing different temperature values of the surface under study, IRT is a technique with a wide range of applications [26]: (1) civil engineering and buildings [1, 15, 17-19, 22], (2) IRT applied to different types of material [22, 27-33], (3) industrial applications [34-36], (4) environment [37-39] and (5) biomedical applications [40-43]. In the following subsection, a brief review with regard to the most recent IRT works that detect moisture areas affecting the surfaces of different construction materials is described.

2.1. IRT works for detection of moisture areas affecting construction material surfaces

IRT detects moisture areas regardless of the existence of algae or plant growth, or of the changes in visible colour observed in the affected material. This is because IRT analyses the difference between the temperature values of moisture areas and their unaltered environments [16] in the surface of each construction material under study, existing always a significant difference due to the following two physical phenomena that occur in a moist area: (1)

Evaporative cooling/Condensation process at the moist area and (2) Increased heat storage capacity of the moist material.

Among the most recent IRT works, some research increase the surface temperature variations between moisture areas and unaltered surroundings by means of solar radiation, air temperature and wind (passive IRT). On the other hand, the use of artificial sources for the thermal excitation of the target (active IRT), such as lamps and laser pulses, helps for a more controlled environment and heat transfer. Furthermore, both types of acquisition procedures help to detect (qualitative IRT) and also characterize (quantitative IRT) the moisture areas under study.

In spite of the methodologies and the potential of IRT for qualitative IRT, all existing IRT studies require the interpretation of the data by a human operator, as discussed in the Introduction section, except for the IRT work [17]. Automation is the issue, even for quantitative approaches, which still requires special attention from the scientific community for the elaboration of well-defined methodologies [44]. Besides, all the IRT research either employ image processing algorithms specifically developed for thermal images, or do not employ any image processing algorithm. All this is demonstrated by representing, in Table 1, the most recent IRT works within the field of study of this paper, showing the innovative contribution of the methodology developed in this work.

Work [Ref.]	Acquisition procedure	Post-acquisition procedure	Surfaces of construction materials	Automated process	Image processing techniques
Edis et al. [1]	Passive	Quantitative	White glazed ceramic material corresponding to several exterior walls	No	PCT (specific to thermal images)
Garrido et al. [17]	Passive	Qualitative	White plaster material corresponding to various interior walls	Yes	PCT (specific to thermal images)

Barreira et al. [44]	Passive	Qualitative	Zinc plate, XPS, cork, orange ceramic tile, grey ceramic tile, plywood, pine, beech, rendering, green/white lacquered aluminium, marble and galvanized steel materials. Limestone material, and one-coat mortar material, corresponding to a full-scale wall in laboratory conditions and exterior walls, respectively	No	-
Edis et al. [45]	Passive	Quantitative	White glazed ceramic material corresponding to several exterior walls	No	-
Cadelano et al. [46]	Active	Quantitative	Brick, marble and standstone materials corresponding to an interior wall	No	PPT (specific to thermal images)
Georgescu et al. [47]	Passive	Qualitative	Stone material corresponding to interior walls	No	-

Table 1 Review of the most recent IRT studies in moisture areas detection affecting the surfaces of construction materials

3. Recommended requirements during the acquisition stage and methodology

3.1. Recommended requirements during the acquisition stage

According to [11], there are some recommended guidelines to take into account during the acquisition stage of an IRT study made for the detection of moisture on construction materials, mainly affecting their surfaces.

The first important step is the compilation of all the information available regarding the composition of the construction materials under study, in order to have a clear understanding of the displacement of water in the material and perform a more complete interpretation of the results. Subsequently, additional procedures are recommended, depending on the modality of each IRT research. In the case of this paper, the modality is (1) passive IRT: given that all the construction materials are tested in natural conditions and (2) qualitative IRT: since the objective is to detect moisture areas in an automatic mode and not to make an evaluation of their severity. Thus, the following recommended requirements are provided:

- Each thermal image should contain both dry and moist areas. The reason for this is that the IRT study is based on the comparison between the thermal behaviour of dry and moist zones.

- Sunrise and sunset periods would be the most adequate times for thermal image acquisition in order to capture the maximum variation of the surface temperature between dry and moist areas. These are the times where the two physical phenomena that cause temperature differences are more active: (1) Evaporative cooling/Condensation process at the moist area and (2) Increased heat storage capacity of the moist material. Generally, night-time inspections are suggested for building IRT inspection to allow proper gain of solar heat, to provide stable thermal conditions (steady state), and to avoid false/misleading indications [48, 49]. Nevertheless, the choice of the optimal time period for data acquisition depends on the characteristics of the material analysed and its location/orientation. For instance, IRT inspections of glazed ceramic claddings are better in the evening or in the middle of the night, rather than in the morning or in the middle of the day. The reason is that, although the temperature difference between the dry and moist areas is greatest around midday, it only stays at its maximum for a short time while, at night, the temperature difference is smaller but remains stable for longer. In addition, the temperature difference between dry and moist areas observed in the evening is greater than that observed in the morning [45].

- In case of critical conditions, such as relative humidity (RH) higher than 80% and air temperature below 6-7 ºC, there are some solutions to increase the level of evaporative cooling to improve the measurements, such as increasing ambient temperature in order to decrease RH.

3.2. Methodology

The methodology is designed to work with one thermal image at a time, and its workflow is indicated in Fig. 1.

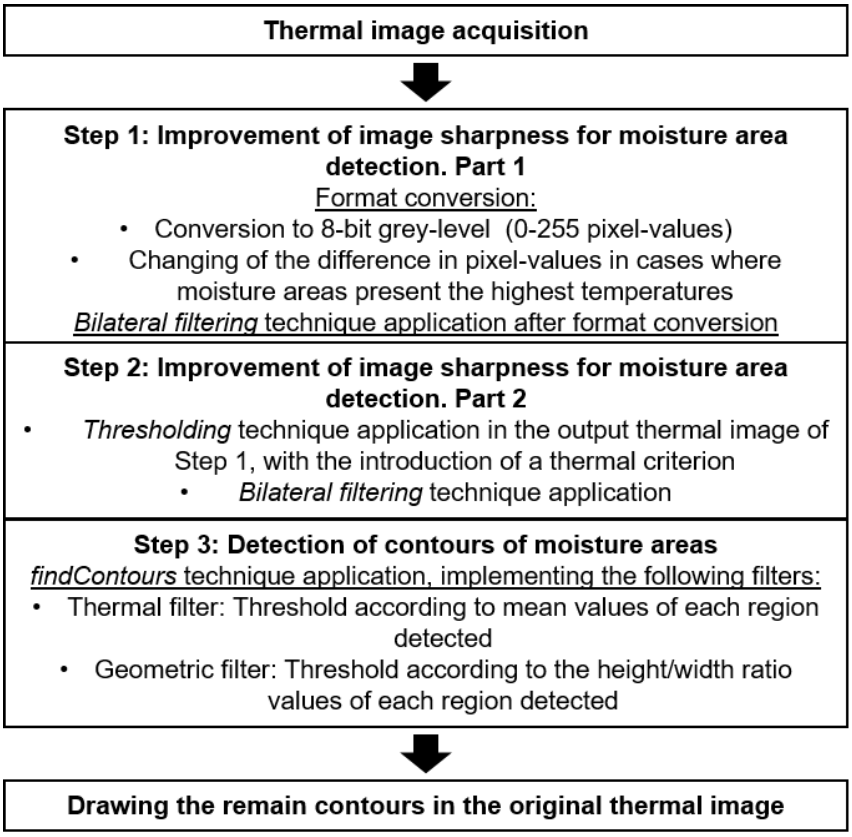

Fig. 1 Workflow of the methodology

All the algorithms were developed and tested by Python 2.7 using Spyder as the Interactive Development Environment (IDE).

3.2.1. Step 1

<u>Format conversion</u>

This methodology works with grayscale images with 256 pixel-values in the interval 0 @ 255 (8-bit format), so the lowest temperature value will be zero (black pixels provided the grayscale palette is applied) and the highest temperature value will be 255 (white pixels provided the grayscale palette is applied). Therefore, the use of equation (1) is necessary to convert the matrix of the input thermal image from temperature values (with temperature units: K, ºC or ºF) to the desired format:

$$I_{(i,j)} = \frac{255 * \left(T_{(i,j)} - T_{min}\right)}{\left(T_{max} - T_{min}\right)} \tag{1}$$

where $T_{(i,j)}$ is the temperature value, with temperature units, at position (*i,j*), T_{max} is the maximum temperature in the temperature matrix, with temperature units, T_{min} is the minimum temperature in the temperature matrix, with temperature units, and $I_{(i,j)}$ is the grey-level intensity at position (*i,j*).

In addition, this methodology only detects contours of moisture areas if the pixel-values of their areas are the lowest values within the thermal image. Then, in the cases where they are the highest, for example, when the material surface is cooled (see the "temperature assumption" of Section 3.2.2.), the values of the image matrix must be reversed with equation (2):

$$I_{new(i,j)} = \left|I_{(i,j)} - 255\right| \tag{2}$$

where $I_{(i,j)}$ is the grey-level intensity at position (*i,j*) before being reversed and $I_{new(i,j)}$ is the grey-level intensity at position (*i,j*) after being reversed.

Bilateral filtering technique implementation

After the previous format conversion, the automatic part of the process begins. It starts with the application of the *bilateral filtering* technique in the thermal image with the desired input format.

This technique is a non-linear function [50], which is highly effective at noise removal while preserving edges in the input image. It has recently been used, for example in [51], to smooth images in order to automatically detect the studs of an interior partition. To do this, the intensity value in each pixel of the image is replaced by a weighted average. This weighted average is based on a Gaussian distribution in space, which ensures that only the pixels close to the pixel under study are considered within its neighbourhood, and another Gaussian filter depending on the difference in pixels, which ensures that only those pixels with an intensity similar to the pixel under study are considered as "blurring". Therefore, the edges of the images are preserved, since the pixels in the contours of objects will have a great variation in intensity with respect to their surroundings [52].

In this way, *bilateral filtering* eliminates the majority of the possible existing noise in the thermal image of the construction material surface, keeping the contours of the moisture areas. On the other hand, *bilateral filtering* is mathematically represented by equation (3):

$$dst(x,y) = \frac{1}{\sum_{x_i,y_i} f_r(\|src(x_i,y_i) - src(x,y)\|) * g_s(x_i - x, y_i - y)} \sum_{x_i,y_i} [src(x,y) * f_r(\|src(x_i,y_i) - src(x,y)\|) * g_s(x_i - x, y_i - y)] \quad (3)$$

where x, y are the coordinates of the current pixel to be filtered and x_i, y_i are the coordinates of the pixel neighbourhood that is used during filtering and defined by argument *d*.

The values of all the arguments are the following:

Argument	Value
src - Source 8-bit or floating-point, 1-channel or 3-channel image	Thermal image input
dst - Destination image of the same size and type as *src*	Thermal image output
d - Diameter of each pixel neighbourhood that is used during filtering (filter mask)	9
sigmaColor - Filter sigma in the intensity space (gaussian function f_r)	75
sigmaSpace - Filter sigma in the coordinate space (gaussian function g_s)	75

Table 2 Values of the arguments to use in the *bilateral filtering* technique

The numerical values of *d*, *sigmaColor* and *sigmaSpace* are established according to the documentation of the OpenCV library available on the web [53]. The value 9 in the diameter of each pixel neighbourhood is recommended for offline applications that need heavy noise filtering. Concerning sigma values, if they are small (< 10), the technique will not have much effect, whereas if they are large (> 150), it will have a very strong effect, making the image look exaggerated. Therefore, a value of 75 is established as an intermediate solution.

3.2.2. Step 2

In this second step, the difference in the pixel-value between the moisture areas and the unaltered zone is increased with the application of a *thresholding* technique. For that, a thermal criterion is introduced, based on a temperature and a thermal assumption:

Temperature assumption

- If the surface of a construction material affected by moisture begins to cool down, the temperature in the moist area is higher than in its surroundings. This fact is due to the condensation process in the moist area, which is an exothermic reaction inducing an increase on the surface temperature of the anomaly with respect to its surroundings, and to the increased heat storage capacity of the moist material.

- If the surface of a construction material affected by moisture begins to heat up, the temperature in the moist area is lower than in its surroundings. This fact is due to the evaporative cooling in the moist area and to the increased heat storage capacity of the moist material. Evaporative cooling is an endothermic reaction inducing a decrease on the surface temperature of the pathology with regard to its surroundings.

Thermal assumption

This assumption is referred to the distribution of the temperatures in the thermal image. Typically, the total number of pixels belonging to moisture areas affecting the surface of a construction material is much lower than the total. Taking this into account and knowing that the pixel-values of the moist areas are considerably lower/higher than those of the pixels associated to the unaltered surface of the material under study according to the previous temperature assumption, the distribution of the temperatures (the histogram of the pixel-values) of the thermal image can be assimilated to a pseudo-bimodal distribution. Thus, in the case of moisture, the thermal image histogram shows one Gaussian distribution consisting of the general distribution of the pixel-values of the unaltered zone of the material and other Gaussian distribution formed by the pixels of the existing moisture areas. The maximum peak of the first distribution is considerably higher than the peak of the second distribution. In addition, the reason for the prefix “pseudo-” is because the thermal image histogram is a combination between a normal or Gaussian distribution and a bimodal Gaussian distribution. A bimodal distribution presents two normal distribution curves combined and two maximum peaks with similar magnitude, which are the two most common/repeated pixel-values.

A demonstration of this thermal assumption can be seen in Fig. 2, corresponding to the histogram of the output thermal image of the Step 1 belonging to one of the surfaces of the construction materials analysed in Section 4 (Material_1). All other construction materials tested presented a similar distribution.

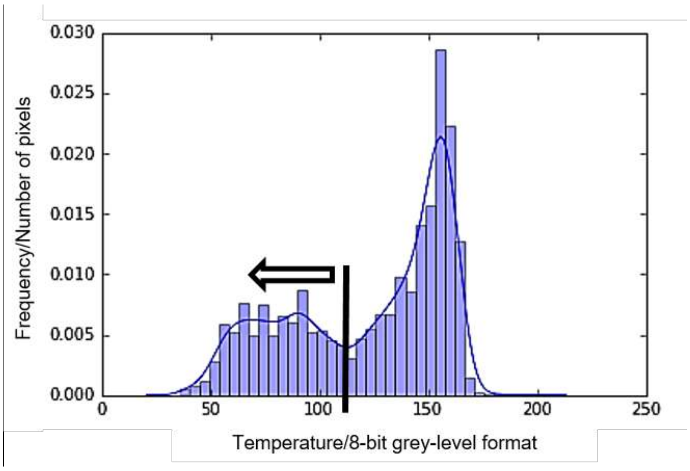

Fig. 2 Histogram of the thermal image of one of the surfaces of construction materials analysed in Section 4, Material_1, after the Step 1 (the arrow indicates where the moisture pixels would be located)

With the purpose of evaluating whether the histogram in Fig. 2 is really a pseudo-bimodal distribution, a polynomial fit is performed on that histogram to confirm if there are two Gaussian bells and whether the maximum peak of the unaltered zone is considerably larger than the maximum peak of the moisture areas. For that, this polynomial has to be assimilated to the blue line of Fig. 2, as that line represents the shape of the histogram under study. Fig. 3 shows this polynomial (green line) with regard to the blue line. For the adjustment, the minimum value of the coefficient of determination (R^2) is established to 0.8, based on the level used in [1]. When the minimum value is reached, the correlation between the two lines is classified as acceptable “strong”. Indeed, the R^2 obtained in Fig. 3 was 0.84.

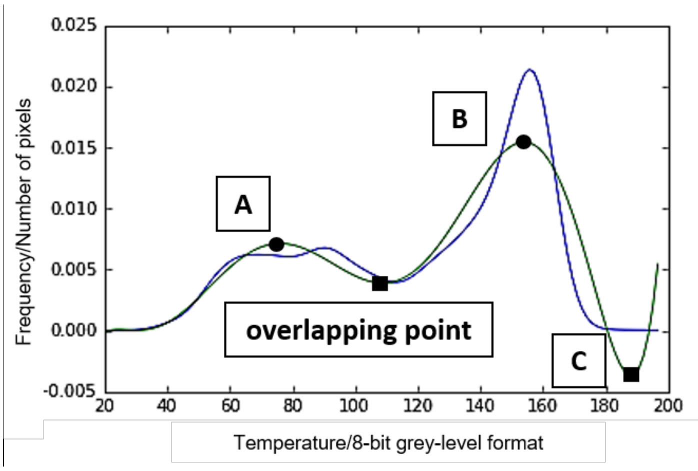

Fig. 3 Polynomial fit (green line) with regard to the line representing the shape of the histogram in Fig. 2 (blue line). The circular (letters: "A" and "B") and rectangular (sentence "overlapping point" and letter "C") symbols represent the relative maximum and minimum points of the polynomial, respectively

Regarding the relative maximum points calculated for the polynomial fit in Fig. 3, two values are observed in the following positions (letters: "A" and "B"): (76.068, 0.007) for "A" and (153.985, 0.015) for "B". As the ratio of "B"/"A" is approximately equal to 2 according to the values along the vertical axis, it can be stated that effectively: (1) there are two maximum peaks ("A" and "B") and, (2) the maximum peak, "B", belongs to the normal distribution curve of the unaltered zone of the Material_1, being twice its magnitude than the maximum peak "A", which belongs to the normal distribution curve of the moisture areas.

Moreover, an overlap between the Gaussian distributions of the unaltered zone and the moisture areas can be observed approximately at the minimum point located in the centre of the polynomial in Fig. 3 (named "overlapping point"). *Overlapping point* represents approximately the pixel-value of the contours of the moisture areas of the Material_1, i.e., it is the equivalent to the starting point of the arrow in Fig. 2.

Finally, the demonstration of Gaussian distributions is possible by calculating the Skewness and Kurtosis values of each distribution before the *overlapping point*, based on the blue line of Fig. 3. With the computation of these parameters, it is possible to prove whether a distribution is a normal/Gaussian curve. For that, the Skewness and the Kurtosis values must be 0 and 3, respectively [54]. According to [55], a range of -2 @ +2 with regard to the optimal values is acceptable for testing whether a distribution is normal/Gaussian. In this case, the values obtained are represented in the following table (Table 3):

Distribution	Skewness	Kurtosis
Moisture areas	-0.54	1.58
Unaltered zone	0.67	2.30

Table 3 Skewness and Kurtosis values of each distribution (blue line) of the histogram of the Fig. 3 before/after *overlapping point* regarding moisture areas/unaltered zone distributions, respectively

Skewness and Kurtosis computations have been performed using the corresponding functions of Python 2.7. [56, 57], and valid results have been obtained, demonstrating the Gaussian distribution of both the moisture areas and the unaltered zone.

Thresholding technique implementation and second application of *bilateral filtering* technique

According to the previous theoretical assumptions, the *overlapping point* represents an important value, since it belongs approximately to the contours of the moisture areas in the thermal image. Therefore, the *thresholding* technique will give more weight to the pixel-values of the thermal image that are below the value of the *overlapping point*, since, due to the format conversion of Step 1, moisture areas are always going to present lower temperature than unaltered areas.

At first glance, the use of the Otsu method, a *thresholding* technique specifically developed for visible images, seems to be the most appropriate for determining the *overlapping point*, as it works very well for finding the overlap point in images with bimodal distributions. However, according to [58], if the histogram of an image is a pseudo-bimodal distribution, the identification of the *overlapping point* can be quite inaccurate. This occurs in inspection applications on objects that contain small defects, with much smaller areas than the defect-free areas. An example can be seen in [59], and the same happens in thermographic inspections of materials with small anomalies, as in the case of this study.

So, the thermal criterion is considered with the objective of obtaining the *overlapping point* instead of applying the Otsu method, but leaving the remaining steps of said method intact. The total steps of the *thresholding* technique of this paper would be as follows:

(1) The *overlapping point* is calculated by the thermal criterion, and is taken as the reference threshold value.

(2) All pixel-values of the thermal image histogram that are below the value of the *overlapping point* are equaled to zero and the rest are subtracted by the *overlapping point* value.

(3) The resulting pixel-values are multiplied by a scale. This scale consists of the division of 255 between the differences of the maximum pixel-value of the output thermal image of the Step 1, minus the *overlapping point* value obtained. The number 255 in the numerator is the result of the difference of the new range of pixel-values of the thermal image after this step (which will always be [0-255] since uint8 format is the format working in this methodology).

(4) The resulting pixel-values that are above 255 are equaled to 255.

Regarding the basis of the thermal criterion, it consists of calculating the optimal combination of the arithmetic mean, $\overline{x}$, and the standard deviation, *s*, of the pixel-values of the output thermal image of the Step 1. The reasons for using $\overline{x}$ and *s* instead of applying polynomial adjustment in the thermal image histogram are because it is a more direct way of obtaining the *overlapping point* and that the values of both parameters partly depend on the Gaussian bell of the moisture areas: (1) $\overline{x}$ parameter is partially dependent on the height of that bell and, (2) *s* parameter is partially dependent on its width. In addition, in this way, the *overlapping point* is obtained in an automated mode.

Fig. 4 represents the histogram of the thermal image of Fig. 2, with the ideal *overlapping point* indicated along the horizontal axis, where the $\overline{x}$ and *s* values of the thermal image are shown with marks, also along the horizontal axis, according to the following results: $\overline{x}$-0.5**s*, $\overline{x}$-*s* and $\overline{x}$-1.5**s*.

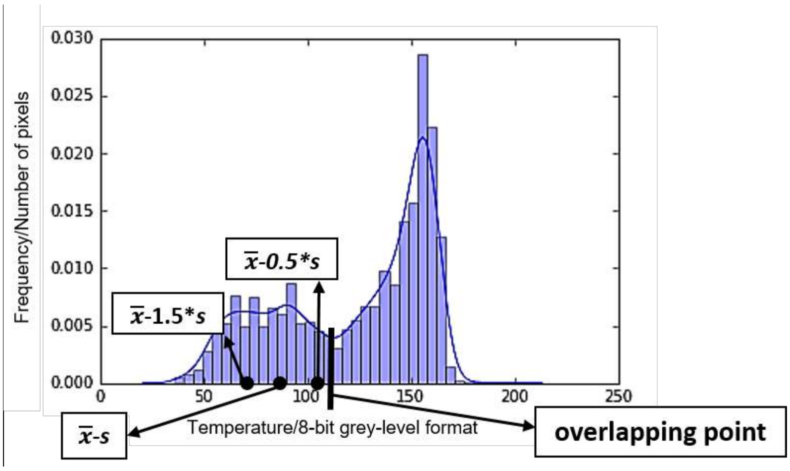

Fig. 4 Histogram of the thermal image of Fig. 2 indicating the $\bar{x}$-0.5*s, $\bar{x}$-s and $\bar{x}$-1.5*s values of the thermal image by black points (the vertical black line indicates the ideal *overlapping point*)

$\bar{x}$-0.5*s is the combination closest to the ideal *overlapping point*, showing in Fig. 5 the result after applying the Step 1 and the *thresholding* technique with the $\bar{x}$-0.5*s combination.

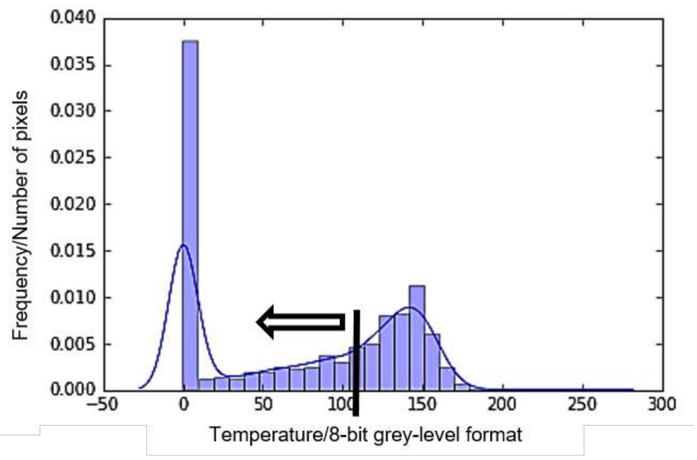

Fig. 5 Histogram of the thermal image of Fig. 2 after the Step 1 and the *thresholding* technique with the $\bar{x}$-0.5*s combination (the arrow indicates where the moisture pixels would be located)

Comparing with the original histogram, this histogram has been stretched along the higher pixel-values, while the lower pixel-values have been contracted, giving greater weight to the lower area with regard to the rest of the histogram of the thermal image.

On the other hand, although the result of the Otsu method [60] in the histogram of Fig. 4 is also a point close to the ideal *overlapping point* (with a value of 113 along the horizontal axis, similar to the 105 of the $\bar{x}$-0.5*s combination, being 110 the value of the ideal *overlapping point*), it is not a consistent result for all cases. For example, in the case of Material_42, which presents a temperature distribution less similar to an ideal bimodal distribution, the Otsu method is less precise than the thermal criterion of this methodology, in this case the $\overline{x}$-0.5*s combination, showing its limitation for this study (see Fig. 6).

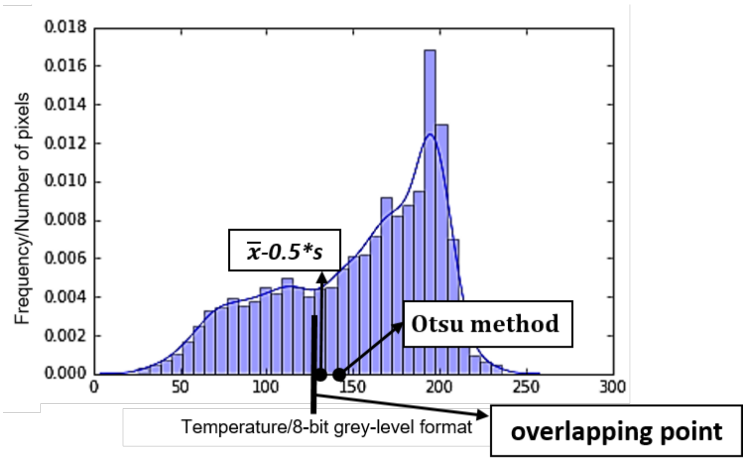

Fig. 6 Histogram of the thermal image of one of the construction materials analysed in Section 4, Material_42, after the Step 1 (“overlapping point” represents the ideal point)

As last action to perform in Step 2, the *bilateral filtering* technique is applied again, allowing to emphasize the contours of the existing moisture areas after the *thresholding* technique.

In Section 4, in order to obtain preliminary results, a comparison is performed between the final results of the methodology (Step 1 + Step 2 + Step 3), applying the following different combinations to obtain the *overlapping point*, from several surfaces of construction materials: (1) $\overline{x}$-1.5*s, (2) $\overline{x}$-s and (3) $\overline{x}$-0.5*s. So, the same variables ($\overline{x}$ and s) and math operation (subtraction, “-“) are applied to all thermal images.

3.2.3. Step 3

The aim of the final step of the methodology is to draw the contours of the candidates to moisture areas on the original thermal image.

To do this, changes in the pixel-value level are searched in the thermal image processed up to this point. Specifically, the objective is to classify as contours the pixels that are located around the *overlapping point* value according to the selected combination of $\overline{x}$ and s. In other words, the task is to detect the pixels of the border of the darkest areas of the image, which are the possible candidates to be moisture areas, grouping the pixels detected in various vectors (*contours*) in order to separate the different areas found. For this, *findContours* technique of OpenCV [50] is used with the implementation of a geometric and a thermal filter, in order to remove false positives. The filters work in this way:

(1) The thermal filter is based on the fact that the pixel-values of moisture areas are located below the *overlapping point* value according to the combination of $\overline{x}$ and *s* selected. Therefore, the *contours* computed by the *findContours* technique that surround an area with an average pixel-value (after Step 1) higher than the *overlapping point* are discarded as moisture candidates.

(2) Regarding the geometric filter, the geometry of an area with moisture is considered as not perfect square, because this happens only under very specific conditions. So, *contours* with a height/width ratio value equal to 1 are discarded as moisture areas since they are probably noise that has not been removed by the *bilateral filtering* technique or any artefact present in the thermal image.

Therefore, the *contours* that remain are drawn in the original thermal image.

4. Evaluation of the methodology

4.1. Selection of construction materials for the analysis of their surfaces

The methodology was tested in different surfaces of several types of construction materials, selected among the types with highest use. One is synthetic tesserae (which is a sort of molten glass) usually used to build mosaic samples for decoration purposes; another is wood (beech) analysed from different directions of the fibres (radial, tangential and axial directions); and two tests are performed in different appearances of typical concrete belonging to outdoor: one in a building façade and one in a bridge. Likewise, the samples analysed in [17], made of white plaster typical of surfaces belonging to the interior of residential buildings, were also tested and compared with the previous study.

The descriptions and properties of the types of construction materials used for testing the methodology in their surfaces are presented in Table 4. The numerical values were obtained from the materials' technical specifications under ambient conditions and at room temperature.

Reference	Type of construction material	Emissivity	Thermal conductivity/W $*m^{-1} K^{-1}$	Density/kg* m^{-3}	Specific heat capacity/J $*kg^{-1} K^{-1}$
Material_1	Synthetic tesserae	0.93	0.93	2600	670
Material_21	beech (fibres radial direction)	0.94	0.169	750	1413
Material_22	beech (fibres tangential direction)	0.94	0.142	747	1419
Material_23	beech (fibres axial direction)	0.94	0.418	750	1413
Material_31	Concrete	0.85	1.28	2300	880
Material_32	Concrete	0.85	1.28	2300	880
Material_41	White plaster	0.90	0.17	800	1000
Material_42	White plaster	0.90	0.17	800	1000
Material_43	White plaster	0.90	0.17	800	1000

Table 4 Description and properties of the construction materials under study in environmental conditions and at room temperature

The construction materials are named with different nomenclature. The first number identifies the type of material, and the second number exists if there is more than one example of the same type of material tested.

4.2. Thermographic inspection for moisture detection

Despite the description of the ideal plan of acquisition (Section 3.1.), during the tests, the acquisitions were performed under different ambient conditions without necessarily being the recommended ones, checking whether the methodology developed presents a good performance for all of them. For that, two different TIR cameras were used for data acquisition to ensure sensor-independence, while a hygrometer was used to measure the ambient conditions. Regarding TIR cameras, the corrections of emissivity and reflected temperature are performed before each measurement, as well as ambient compensation. Although this paper works in qualitative IRT, it is necessary to have the most realistic histogram possible for each thermal image under study because it is very important to get the *overlapping point* as close as possible to the ideal value. The main specifications of the TIR cameras used are described in Table 5.

	TIR camera 1	TIR camera 2
Sensor type	Uncooled focal plane array (µbolometer)	Uncooled focal plane array (µbolometer)
Thermal image/pixels	320 (H) x 240 (V)	640 (H) x 480 (V)
Resolution/ºC	0.1	0.1
Accuracy	± 2 ºC or ± 2% of reading, whichever is greater	± 2 ºC or ± 2% of reading, whichever is greater
Spectral ranges/µm	7.5 @ 13.5	8 @ 14

Table 5 Specifications of TIR cameras used during the tests

The tests of the surfaces of Material_1, Material_21, Material_22 and Material_23 were performed under the same conditions, inside a laboratory where the last three pieces had a weight about 27 grams and with a water content of 15 ml each (around 60% of moisture in the materials). The environment conditions during the tests were: ambient temperature of 19 ºC and RH of 40% approximately, and the TIR camera used was the TIR camera number 1. Fig. 7 shows the surface of these materials in dry conditions.

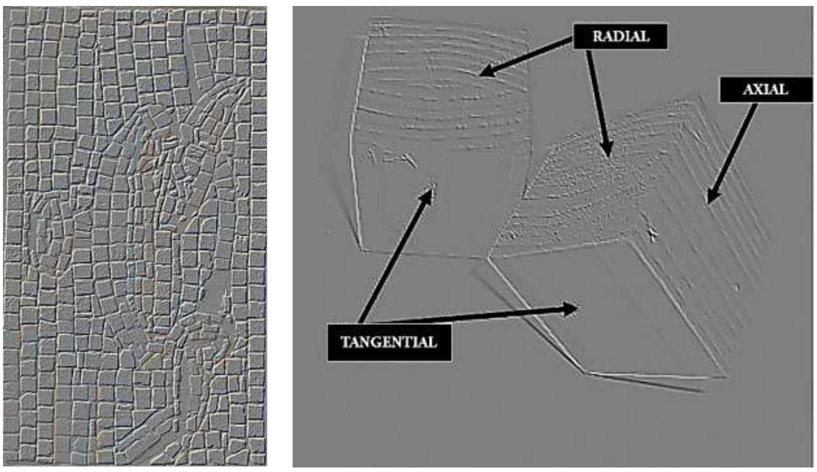

Fig. 7 Investigated materials. Left: Material_1. Right: Indication of the Material_21 “RADIAL”, Material_22 “TANGENTIAL” and Material_23 “AXIAL” directions (all in dry conditions in the figure)

Material_31 belongs to a building façade. In this case, the environment conditions during the test of its surface were: ambient temperature of 17.9 ºC and RH of 72% approximately, and the TIR camera used was the TIR camera number 2. Fig. 8 shows the surface of this material in real conditions (it can be observed that the surface has indications of being affected by moisture).

Fig. 8 Investigated material. Material_31 in real conditions

The Material_32 belongs to two zones of a pillar of a bridge. The environment conditions during the testing of their surfaces were: ambient temperature of 9 ºC and RH of 90% approximately, on a winter day, and the TIR camera used was again TIR camera number 2. Fig. 9 shows the surfaces of this material in real conditions (it can be observed that the surfaces have indications of being affected by various moisture areas).

Fig. 9 Investigated material. Material_32 in real conditions (red circles indicate the selected zones to analysis, “left” and “right” areas)

Finally, the tests of the surfaces of the Material_41, Material_42 and Material_43 were performed under the same conditions, in different interior residential buildings, according to the recommendations given in [17]. The environment conditions during the tests were: ambient temperature of 23 ºC and RH of 50% approximately, and the TIR camera used was the TIR camera number 2. Fig. 10 shows the surfaces of these materials in real conditions (it can be observed that the surfaces have signs of moisture areas).

Fig. 10 Investigated materials. From left to right: Material_41, Material_42 and Material_43 in real conditions (red circles indicate the zones selected for analysis). Reference [17]

4.3. Preliminary results and discussion

Fig.11 shows the thermal images obtained for each construction material surface analysed and affected by moisture areas, in grayscale, except for the surfaces of the materials tested in [17] that are in RGB to maintain the format used in that work and evaluate the colour-independence of the methodology. Temperature scales are in ºC.

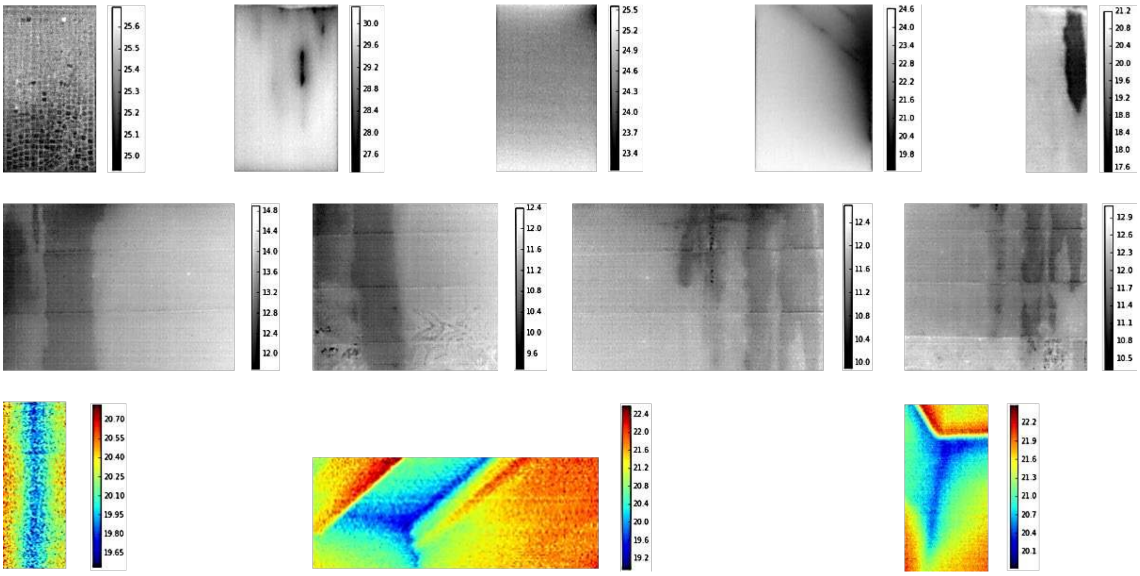

Fig. 11 Thermal images of the surfaces of the construction materials under study. From left to right and from top to bottom, surfaces of the: Material_1, Material_21, Material_22, Material_23, Material_31, Material_32 “left” area (top), Material_32 “left” area (bottom), Material_32 “right” area (top), Material_32 “right” area (bottom), Material_41, Material_42 and Material_43 (from reference [17]). The temperature scale (ºC) is shown at the right of each image

On the other hand, Fig. 12 shows the results using the methodology for automatic moisture detection (red lines), with different combination of $\bar{x}$ and *s* for the computation of the *overlapping point,* in order to evaluate preliminary results: (1) $\bar{x}$-1.5**s*, (2) $\bar{x}$-*s* and (3) $\bar{x}$-0.5**s*. It should be noted that if it was not for Steps 1 and 2, no moisture area would be detected with Step 3, or only moisture areas with one dimension (points).

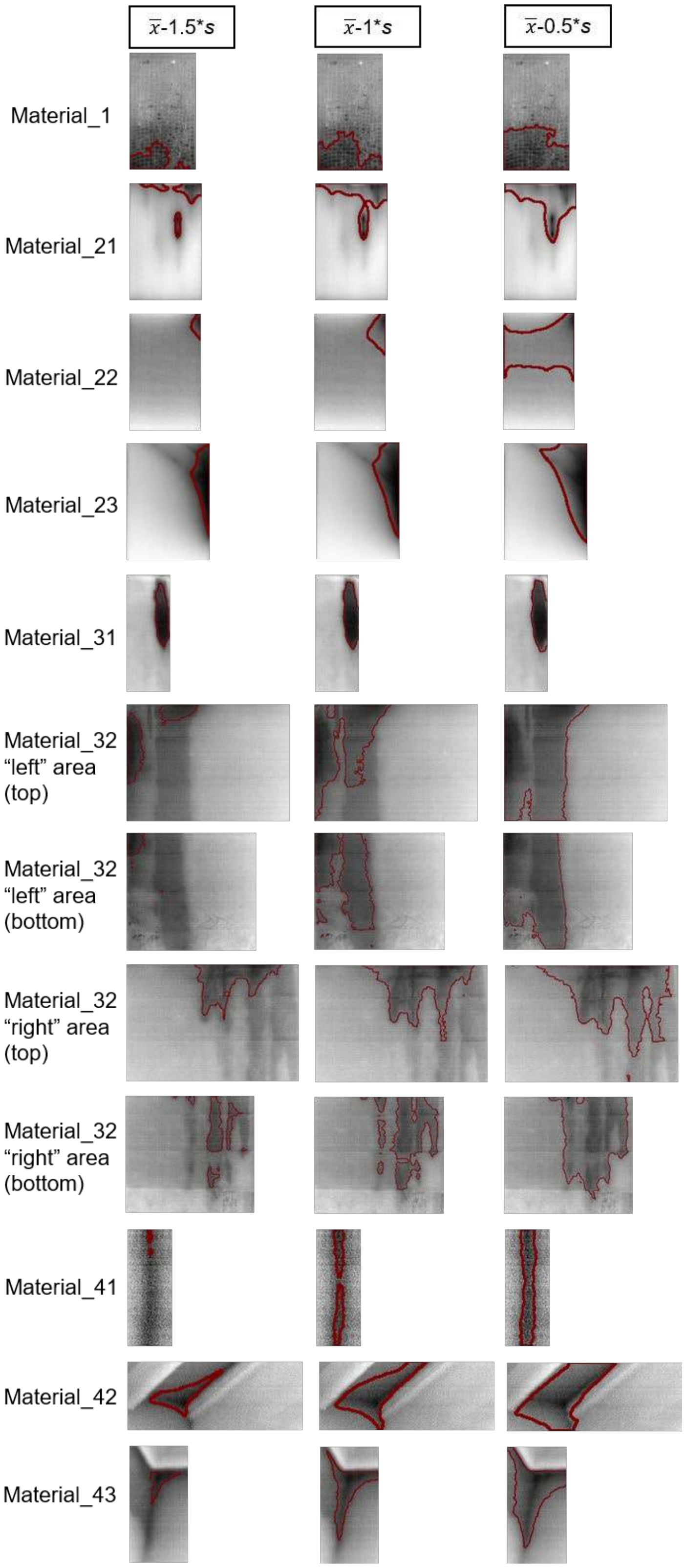

Fig. 12 Preliminary results of the methodology. From left-column to right-column: 1) $\bar{x}$-1.5*s, 2) $\bar{x}$-1*s and 3) $\bar{x}$-0.5*s

Fig.13 shows the real contours of the existing moistures in each construction material surface (red lines) detected by the operator during the IRT inspections. From the Fig.13, it is possible to compute various performance metrics with the finality of evaluating the accuracy of this methodology and comparing the results of the different combinations of $\overline{x}$ and s for the computation of the *overlapping point* among the 3 options of Fig. 12.

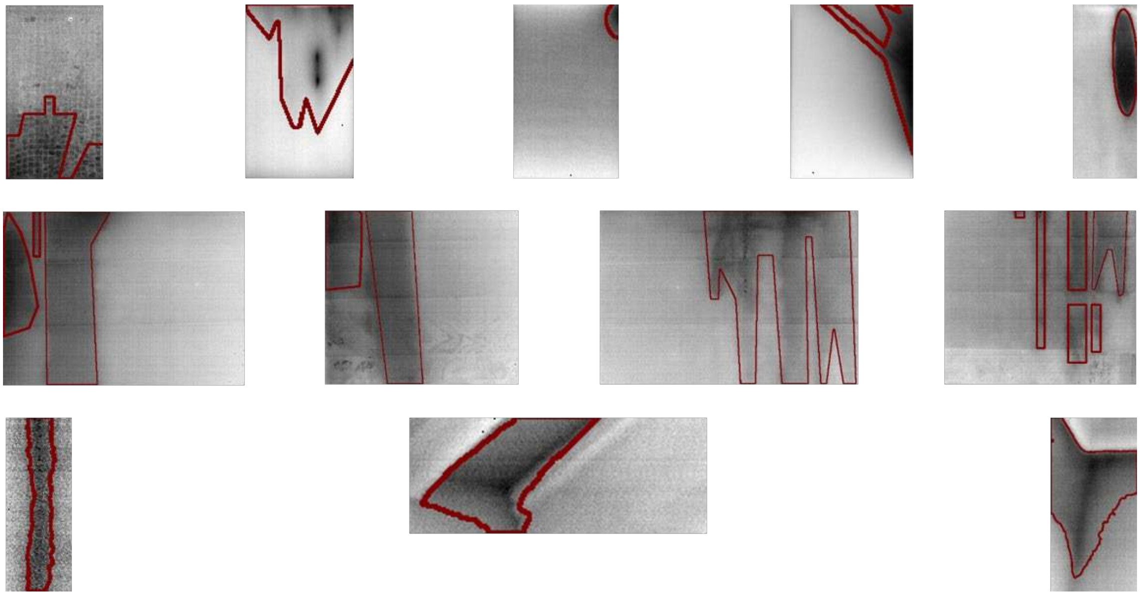

Fig. 13 Real contours of the existing moistures in the thermal images of each construction material surface (red lines). From left to right, top to bottom, surfaces of the: Material_1, Material_21, Material_22, Material_23, Material_31, Material_32 “left” area (top), Material_32 “left” area (bottom), Material_32 “right” area (top), Material_32 “right” area (bottom), Material_41, Material_42 and Material_43 (from reference [17])

The most adequate combination will be the one with the most pixels inside each contour calculated in common with the pixels of the real moisture areas (number of true positives) and with the least pixels unclassified as wet pixels (number of false negatives). For that, the following performance metrics are defined, as in reference [17]:

$$Precision = \frac{TP}{TP + FP} \quad (4)$$

$$Recall = \frac{TP}{TP + FN} \quad (5)$$

$$F - score = 2 * \frac{Precision * Recall}{Precision + Recall} \quad (6)$$

where *TP*, *FP* and *FN* are the number of true positives, false positives and false negatives, respectively. Results of *precision*, *recall*, and *F-score* performance metrics are shown in Table 6 for the three combinations of parameters under study in each construction material surface.

Material reference	Combination	Precision/%	Recall/%	F-score/%
1	$\bar{x}-1.5*s$	100	38	55
	$\bar{x}-1*s$	95	67	79
	$\bar{x}-0.5*s$	83	94	88
21	$\bar{x}-1.5*s$	100	17	28
	$\bar{x}-1*s$	100	33	50
	$\bar{x}-0.5*s$	99	51	67
22	$\bar{x}-1.5*s$	91	92	91
	$\bar{x}-1*s$	37	99	54
	$\bar{x}-0.5*s$	9	99	17
23	$\bar{x}-1.5*s$	100	57	73
	$\bar{x}-1*s$	90	81	85
	$\bar{x}-0.5*s$	67	92	77
31	$\bar{x}-1.5*s$	99	67	80
	$\bar{x}-1*s$	98	84	91
	$\bar{x}-0.5*s$	94	96	95
32 “left” area (top)	$\bar{x}-1.5*s$	100	25	40
	$\bar{x}-1*s$	87	64	73
	$\bar{x}-0.5*s$	75	98	85
32 “left” area (bottom)	$\bar{x}-1.5*s$	100	7	14
	$\bar{x}-1*s$	86	70	77
	$\bar{x}-0.5*s$	71	92	80
32 “right” area (top)	$\bar{x}-1.5*s$	99	25	40
	$\bar{x}-1*s$	94	37	53
	$\bar{x}-0.5*s$	88	58	70
32 “right” area (bottom)	$\bar{x}-1.5*s$	88	30	45
	$\bar{x}-1*s$	75	71	73
	$\bar{x}-0.5*s$	54	92	68
41	$\bar{x}-1.5*s$	100	3	7

	$\bar{x}$-1*s	100	34	51
	$\bar{x}$-0.5*s	100	81	90
42	$\bar{x}$-1.5*s	100	26	42
	$\bar{x}$-1*s	100	53	69
	$\bar{x}$-0.5*s	100	88	94
43	$\bar{x}$-1.5*s	100	10	19
	$\bar{x}$-1*s	100	59	74
	$\bar{x}$-0.5*s	100	64	78

Table 6 *Precision*, *recall* and *F-score* for the three combinations analysed in each construction material surface

Due to the great amount of information presented in the previous table, Table 7 shows the average and standard deviation values of each performance metric parameter for each combination.

Performance metrics		Combination		
Parameter		$\bar{x}$-1.5*s	$\bar{x}$-1*s	$\bar{x}$-0.5*s
Precision/%	Average/%	**98**	*89*	78
	Standard deviation/%	**4**	*17*	25
Recall/%	Average/%	33	*63*	**84**
	Standard deviation/%	25	*20*	**16**
F-score/%	Average/%	45	*69*	**76**
	Standard deviation/%	25	**13**	*20*

Table 7 Average and standard deviation values in each performance metric parameter for each combination considering all the results in Table 6. The first position on average (the highest) and on standard deviation (the lowest) values for each parameter are highlighted in bold, while italics is used for the second position

Table 8 shows the average and standard deviation values of each performance metric parameter according to the TIR camera used with the combination $\bar{x}$-1*s. This combination is selected because of their good average and standard deviation values in all performance metrics (Table 7).

Performance metrics	TIR camera

Parameter		1	2
Precision/%	Average/%	81	**93**
	Standard deviation/%	25	**9**
Recall/%	Average/%	**70**	59
	Standard deviation/%	24	**16**
F-score/%	Average/%	67	**70**
	Standard deviation/%	15	**12**

Table 8 Average and standard deviation values in each performance metric parameter according to the TIR camera used with the combination $\bar{x}$-1**s*, considering all the results in Table 6. The first position on average (the highest) and on standard deviation (the lowest) values for each parameter are highlighted in bold

In light of the results shown in Table 7 and 8, the following conclusions are reached:

- Despite the best average and standard deviation values of the combination $\bar{x}$-1.5**s* in the *precision* parameter, very low values are obtained in the other parameters. Therefore, it is discarded as a good combination for obtaining the *overlapping point*.

- Between the combinations $\bar{x}$-1**s* and $\bar{x}$-0.5**s*, it is observed that the first one obtains better results in the *precision* parameter, although the second combination shows better results for the other two parameters (*recall* and *F-score*). Thus, as preliminary results, it can be stated that the developed methodology gives better results if a combination of $\bar{x}$ and *s* between $\bar{x}$-1**s* @ $\bar{x}$-0.5**s* is established, in order to obtain the *overlapping point*.

- Although each TIR camera used has analysed surfaces of different construction materials, provided that the results are uniform for all cases, it can be said that the type of TIR camera used will not change the effectiveness of the methodology proposed. A good example is the similarity of the results of the *F-score* parameter, which is considered as the most representative parameter since it includes both the *precision* and the *recall* parameters.

In the case that the purpose of the methodology is simply to detect the presence of a possible moisture zone instead of marking its real limits, with the aim at warning the operator of the presence of an anomaly in that area of the construction material surface under study, the quality metrics of the methodology change according to different weights given to the two performance metrics used in the *F-score* parameter. In this case, where focus is set on detection rather than on delimitation, more weight is given to the *precision* parameter. In the original definition of *F-score*, the weights of the *precision* and *recall* parameters are set at 50%. In order to establish a weight of 70% to *precision* and 30% to *recall*, the following equation is used:

$$F - score' = \frac{Precision * Recall}{0.3 * Precision + 0.7 * Recall} \quad (7)$$

And the new *F-score* results with regard to Table 7 are the following (Table 9):

Performance metrics		Combination		
Parameter		$\bar{x}$-1.5*s	$\bar{x}$-1*s	$\bar{x}$-0.5*s
F-score'/%	Average/%	53	*75*	**76**
	Standard deviation/%	25	**13**	*21*

Table 9 Average and standard deviation values in the new *F-score* parameter for each combination considering all the results in Table 6. The first position on average (the highest) and on standard deviation (the lowest) values for each parameter are highlighted in bold, while italics is used for the second position

Despite the improvement of the combination $\bar{x}$-1.5*s from this new point of view, the combination of $\bar{x}$ and s between $\bar{x}$-1*s @ $\bar{x}$-0.5* is still maintained as the most appropriate option. The same results are obtained with weights of 60%/40%, 80%/20% and 90%/10% given to *precision*/*recall* respectively (Table 10):

Performance metrics		Combination		
Parameter		$\bar{x}$-1.5*s	$\bar{x}$-1*s	$\bar{x}$-0.5*s
F-score'/%	Average/%	48	*72*	**76**
(60%/40%)	Standard deviation/%	25	**13**	*21*
F-score'/%	Average/%	60	**78**	*77*
(80%/20%)	Standard deviation/%	24	**13**	*22*
F-score'/%	Average/%	71	**83**	*77*
(90%/10%)	Standard deviation/%	*21*	**14**	24

Table 10 Average and standard deviation values in the new *F-score* parameters (*precision*/*recall* weights (%): (1) 60/40, (2) 80/20 and (3) 90/10) for each combination considering all the results in Table 6. The first position on average (the highest) and on standard deviation (the lowest) values for each parameter are highlighted in bold, while italics is used for the second position

4.3.1. Comparison with existing methodologies

This section compares the preliminary results obtained with this methodology with regard to the construction materials tested in [17], against the results of that study. To that end, Table 11 represents the values of the performance metrics (*F-score* with the weights of the *precision* and *recall* parameters set at 50%) with respect to the surfaces of the Material_41, Material_42 and Material_43; showing the results with the combinations $\bar{x}$-1**s* and $\bar{x}$-0.5**s*, and the results obtained in [17].

Material reference	Methodology	Precision/%	Recall/%	F-score/%
41	$\bar{x}$-1*s	**100**	34	51
	$\bar{x}$-0.5*s	**100**	81	**90**
	Method of [17]	70	**97**	81
42	$\bar{x}$-1*s	**100**	53	69
	$\bar{x}$-0.5*s	**100**	88	**94**
	Method of [17]	84	**89**	86
43	$\bar{x}$-1*s	**100**	59	74
	$\bar{x}$-0.5*s	**100**	64	78
	Method of [17]	91	**82**	**86**

Table 11 *Precision*, *recall* and *F-score* results with regard the materials used in [17], applying the combinations $\bar{x}$-1**s* and $\bar{x}$-0.5**s*, and representing the own results obtained in [17]. The first position on average (the highest) values for each parameter are highlighted in bold

With the methodology developed in this paper, *precision* is gained with regard to the study [17], compensating for the decrease in *recall*. Therefore, with this comparison, it is concluded that:

- The method proposed in [17] is more appropriate for detecting the real extent of each moisture area, although it can be overestimated, provided that the areas are already classified with presence of moisture.

- The methodology described here is more advisable for a first moisture inspection, even if the total of each moisture area is not covered. In other words, this paper detects better whether or not there are moisture areas affecting the surfaces of different construction materials compared to the method [17]. Then, this methodology would be a first application to define possible moisture areas, and in the case of needing more detail, method [17] would be applied.

4.3.2. Visible images for moisture detection

In this section, the results of the visual inspection of moisture areas show that the visual technique does not make possible the detection of moisture areas or presents poor performance. The demonstration of the inadequacy of the visual inspection is performed with the surfaces of the Material_41, Material_42 and Material_43. In addition, although the proposed methodology includes algorithms specifically developed for visible images, the results for the detection of moisture (Fig.14) are also poor.

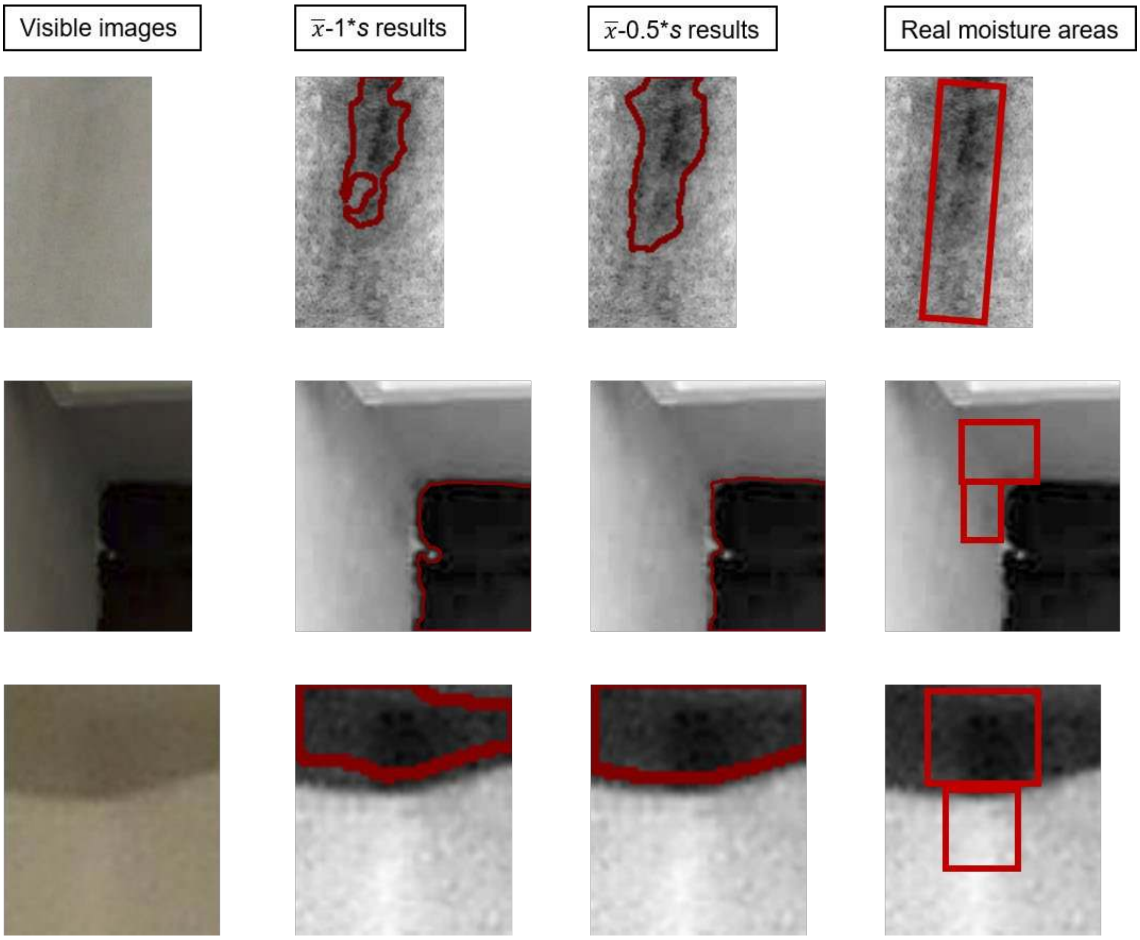

Fig. 14 Demonstration of the non-viability of using visible images to detect moisture areas

5. Conclusions and future perspectives

This work presents a methodology for the automatic detection of moisture areas affecting the surfaces of several construction materials, under different ambient conditions and from thermographic images. This procedure is one of the first methods of these characteristics in the literature, implying a step forward towards the automation of the inspection process and optimization of the decision-taking for rehabilitation actions in damaged materials.

To achieve the purpose of the paper, the methodology introduces the application of three image processing techniques, specifically designed for visible images, to the thermographic images of surfaces of different construction materials. The application of these techniques requires some adaptations of the format of the thermal images and a different use of the techniques. With them, it is possible, first, (1) to increase the difference in the pixel-value between the moisture areas and the unaltered zones (with the *thresholding* technique) and to remove noise while keeping the edges intact (with the *bilateral filtering* technique), and (2) to detect contours of moisture areas according to the highest difference of pixel-value in each thermal image (with the *findContours* technique).

In the case of the *bilateral filtering* technique, a previous format conversion of the thermal images is necessary, while for the *thresholding* technique, a thermal criterion is introduced to establish a threshold value in order to select the pixel-value of the contours of the moisture areas. Regarding the *findContours* technique, a geometric and a thermal filter are applied to the outputs, in order to remove false positives.

The thermal criterion used in the *thresholding* technique is based on the temperature distribution of the thermal images under study, which are assimilated to pseudo-bimodal distributions, with two Gaussian bells combined and with the peak of one bell considerably smaller than the peak of the other. In the thermal criterion, three different combinations are applied in each thermal image under study, in order to obtain the optimal value of the *overlapping point,* which established the separation between the two distributions. These combinations are based on the image parameters corresponding to the arithmetic mean pixel value, $\overline{x}$, and the standard deviation, *s*. The determination of the optimal combination is experimentally performed with 12 different surfaces of construction materials affected by moisture areas and under various environmental conditions, specifically comparing the following combinations: 1) $\bar{x}$-1.5**s*, 2) $\bar{x}$-1**s* and 3) $\bar{x}$-0.5**s*.

The preliminary results show that the best combination is a combination of $\bar{x}$ and *s* established between the combinations $\bar{x}$-1**s* and $\bar{x}$-0.5**s*, with values between 78% @ 89% for *precision*, 63% @ 84% for *recall* and 69% @ 76% for *F-score* parameters. These results show the optimal behaviour of the methodology to just detect the presence of moisture, without recognizing its entire area.

Therefore, the purpose of this paper is fulfilled, since a methodology has been developed in order to detect and draw contours of moisture areas affecting the surfaces of different construction materials analysed during thermographic inspections. In addition, the inspections have been performed under different environmental conditions and the proposed procedure works automatically, showing acceptable results of *precision*, *recall* and *F-score* parameters. Future criteria and techniques can be added for the improvement of the methodology, especially to discern moisture of other pathologies and artefacts that generate dark areas in grayscale thermal images, such as shadows and graffiti painted on walls. So, future research will deal with the implementation of a criterion regarding thermophysical properties of the detected contours, and with the search for the optimal combination of $\bar{x}$ and *s* between the combinations $\bar{x}$-1**s* and $\bar{x}$-0.5**s* testing more types of construction materials.

Acknowledgments

Authors would like to thank the Ministerio de Economía y Competitividad (Gobierno de España) for the financial support given through programs for human resources (FPU16/03950) and TEC2016-76021-C2-2-R (AEI/FEDER, UE). Special thanks to the Cátedra Iberdrola VIII Centenario – University of Salamanca, and European Commission for the funding given through the program H2020-FTIPilot-2015-1 to the proposal 720661 – ENGINENCY. S. Sfarra wants to thank the restorer who assisted him to construct the mosaic sample and realize the wooden samples. This project has received funding from the European Union's Horizon 2020 research and innovation programme under grant agreement No 769255. This document reflects only the author's view and the Agency is not responsible for any use that may be made of the information it contains.

References

1. Edis E, Flores-Colen I, de Brito J. Quasi-quantitative infrared thermographic detection of moisture variation in facades with adhered ceramic cladding using principal component analysis. Build Environ. 2015; doi:10.1016/j.buildenv.2015.07.027.

2. Rosina E, Sansonetti A, Ludwig N. Moisture: The problem that any conservator faced in his professional life. J Cult Herit. 2018; doi:10.1016/J.CULHER.2018.04.022.

3. Andersen B, Frisvad JC, Søndergaard I, Rasmussen IS, Larsen LS. Associations between fungal species and water-damaged building materials. Appl Environ Microbiol. 2011; doi:10.1128/AEM.02513-10.

4. World Health Organization Regional Office for Europe. WHO GUIDELINES FOR INDOOR AIR QUALITY DAMPNESS AND MOULD. http://www.euro.who.int/__data/assets/pdf_file/0017/43325/E92645.pdf?ua=1. Accessed 30 Nov 2018.

5. Sivasubramani SK, Niemeier RT, Reponen T, Grinshpun SA. Assessment of the aerosolization potential for fungal spores in moldy homes. Indoor Air. 2004; doi:10.1111/j.1600-0668.2004.00262.x.

6. Jarvis JQ, Morey PR. Allergic Respiratory Disease and Fungal Remediation in a Building in a Subtropical Climate. Appl Occup Environ Hyg. 2001; doi:10.1080/10473220117482.

7. Lee TG. Health Symptoms Caused by Molds in a Courthouse. Archives of Environmental Health. 2003; doi:10.1080/00039896.2003.11879145.

8. Horner WE, Helbling A, Salvaggio JE, Lehrer SB. Fungal Allergens. Clin Microbiol Rev. 1995; doi:10.1128/CMR.8.2.161.

9. D'Alessandro F, Baldinelli G, Bianchi F, Sambuco S, Rufini A. Experimental assessment of the water content influence on thermo-acoustic performance of building insulation materials. Constr Build Mater. 2018; doi:10.1016/J.CONBUILDMAT.2017.10.028.

10. Kuishan L, Xu Z, Jun G. Experimental Investigation of Hygrothermal Parameters of Building Materials Under Isothermal Conditions. 2008; doi:10.1177/1744259108102832.

11. Rosina E, Ludwig N. Optimal thermographic procedures for moisture analysis in buildings materials. Proc Soc Photogr Instrum Eng [Internet]. 1999; doi:10.1117/12.361015.

12. Rosina E. When and how reducing moisture content for the conservation of historic building. A problem solving view or monitoring approach?. J Cult Herit. 2018; doi:10.1016/J.CULHER.2018.03.023.

13. Johansson P, Svensson T, Ekstrand-Tobin A. Validation of critical moisture conditions for mould growth on building materials. Build Environ. 2013; doi:10.1016/J.BUILDENV.2013.01.012.

14. Riveiro B, Solla M. Non-destructive techniques for the evaluation of structures and infrastructure. London, United Kingdom: Taylor & Francis Ltd; 2016.

15. Suchocki C, Katzer J. Terrestrial laser scanning harnessed for moisture detection in building materials – Problems and limitations. Automation in Construction. 2018; doi:10.1016/J.AUTCON.2018.06.010.

16. Kirimtat A, Krejcar O. A review of infrared thermography for the investigation of building envelopes: Advances and prospects. Energy Build. 2018; doi:10.1016/J.ENBUILD.2018.07.052.

17. Garrido I, Lagüela S, Arias P. Autonomous thermography: towards the automatic detection and classification of building pathologies. 14th Quant InfraRed Thermogr Conf., Berlin, Germany; 2018.

18. Garrido I, Lagüela S, Arias P, Balado J. Thermal-based analysis for the automatic detection and characterization of thermal bridges in buildings. Energy Build. 2018; doi:10.1016/J.ENBUILD.2017.11.031.

19. Ludwig N, Rosina E, Sansonetti A. Evaluation and monitoring of water diffusion into stone porous materials by means of innovative IR thermography techniques. Measurement. 2018; doi:10.1016/J.MEASUREMENT.2017.09.002.

20. Mercuri F, Zammit U, Orazi N, Paoloni S, Marinelli M, Scudieri F. Active infrared thermography applied to the investigation of art and historic artefacts. J Therm Anal Calorim. 2011; doi:10.1007/s10973-011-1450-8.

21. Szeliski R. Computer Vision: Algorithms and Applications. Texts in Computer Science. Springer-Verlag London Limited; 2011.

22. Yousefi B, Sfarra S, Ibarra-Castanedo C, Avdelidis NP, Maldague XP V. Thermography data fusion and nonnegative matrix factorization for the evaluation of cultural heritage objects and buildings. J Therm Anal Calorim. 2018; doi:10.1007/s10973-018-7644-6.

23. Maldague X, Marinetti S. Pulse phase infrared thermography. J Appl Phys. 1998; doi:10.1063/1.362662.

24. Garrido I, Lagüela S, Arias P. Infrared Thermography's Application to Infrastructure Inspections. Infrastructures. 2018; doi:10.3390/infrastructures3030035.

25. Usamentiaga R, Venegas P, Guerediaga J, Vega L, Molleda J, Bulnes F, et al. Infrared Thermography for Temperature Measurement and Non-Destructive Testing. Sensors. 2014; doi:10.3390/s140712305.

26. Kylili A, Fokaides PA, Christou P, Kalogirou SA. Infrared thermography (IRT) applications for building diagnostics: A review. Appl Energy. 2014; doi:10.1016/J.APENERGY.2014.08.005.

27. Rodríguez-Martín M, Lagüela S, González-Aguilera D, Martínez J. Thermographic test for the geometric characterization of cracks in welding using IR image rectification. Automation in Construction. 2016; doi:10.1016/j.autcon.2015.10.012.

28. Rodríguez-Martin M, Lagüela S, González-Aguilera D, Arias P. Cooling analysis of welded materials for crack detection using infrared thermography. Infrared Phys Technol. 2014; doi:10.1016/j.infrared.2014.09.025.

29. Pahlberg T, Thurley M, Popovic D, Hagman O. Crack detection in oak flooring lamellae using ultrasound-excited thermography. Infrared Phys Technol. 2018; doi:10.1016/J.INFRARED.2017.11.007.

30. Cheng C, Shen Z. Time-Series Based Thermography on Concrete Block Void Detection. Construction Research Congress 2018 conference. New Orleands, LA; 2018.

31. Yao Y, Sfarra S, Ibarra-Castanedo C, You R, Maldague XP V. The multi-dimensional ensemble empirical mode decomposition (MEEMD). J Therm Anal Calorim. 2017; doi: 10.1007/s10973-016-6082-6.

32. Sfarra S, Perilli S, Paoletti D, Ambrosini D. Ceramics and defects. J Therm Anal Calorim. 2016; doi:10.1007/s10973-015-4974-5.

33. Aparicio JHV, Arroyo LO, de León HRMP, Herrera JÁO, Arias YAR, González SA, et al. Implementation of the boundary element method for detecting defects by transient thermography on an aluminum plate. J Therm Anal Calorim. 2016; doi:10.1007/s10973-016-5538-z.

34. Mokhtari Y, Gavérina L, Ibarra-Castanedo C, Klein M, Servais P, Dumoulin J, et al. Comparative study of Line Scan and Flying Line Active IR Thermography operated with a 6-axis robot. 14th Quant InfraRed Thermogr Conf. Berlin, Germany; 2018.

35. Venegas P, Durana G, Zubia J, Sáez De Ocáriz I. Advanced Monitoring Systems for Smart Tooling in Aeronautical Industry 4.0. 14th Quant InfraRed Thermogr Conf. Berlin, Germany; 2018.

36. Lopez-Perez D, Antonino-Daviu J. Application of Infrared Thermography to Failure Detection in Industrial Induction Motors: Case Stories. IEEE Trans Ind Appl. 2017; doi:10.1109/TIA.2017.2655008.

37. Gaudin D, Beauducel F, Coutant O, Delacourt C, Richon P, de Chabalier J-B, et al. Mass and heat flux balance of La Soufrière volcano (Guadeloupe) from aerial infrared thermal imaging. J Volcanol Geotherm Res. 2016; doi:10.1016/J.JVOLGEORES.2016.04.007.

38. Tanda G, Migliazzi M, Chiarabini V, Cinquetti P. Application of close-range aerial infrared thermography to detect landfill gas emissions: a case study. J Phys Conf Ser. 2017; doi:10.1088/1742-6596/796/1/012016.

39. Schwarz K, Heitkötter J, Heil J, Marschner B, Stumpe B. The potential of active and passive infrared thermography for identifying dynamics of soil moisture and microbial activity at high spatial and temporal resolution. Geoderma. 2018; doi:10.1016/J.GEODERMA.2018.04.028.

40. Gerasimova E, Audit B, Roux S-G, Khalil A, Gileva O, Argoul F, et al. A Wavelet-Based Method for Multifractal Analysis of Medical Signals: Application to Dynamic Infrared Thermograms of Breast Cancer. Springer, Cham; 2014; doi:10.1007/978-3-319-08672-9_34.

41. Vardasca R, Vaz L, Magalhães C, Seixas A, Mendes J. Towards the Diabetic Foot Ulcers Classification with Infrared Thermal Images. 14th Quant InfraRed Thermogr Conf., Berlin, Germany; 2018.

42. Fernández-Cuevas I, Bouzas Marins JC, Arnáiz Lastras J, Gómez Carmona PM, Piñonosa Cano S, García-Concepción MÁ, et al. Classification of factors influencing the use of infrared thermography in humans: A review. Infrared Phys Technol. 2015; doi:10.1016/J.INFRARED.2015.02.007.

43. Drzazga Z, Binek M, Pokora I, Sadowska-Krępa E. A preliminary study on infrared thermal imaging of cross-country skiers and swimmers subjected to endurance exercise. J Therm Anal Calorim. 2018; doi:10.1007/s10973-018-7311-y.

44. Barreira E, Almeida RMSF, Delgado JMPQ. Infrared thermography for assessing moisture related phenomena in building components. Constr Build Mater. 2016; doi:10.1016/J.CONBUILDMAT.2016.02.026.

45. Edis E, Flores-Colen I, de Brito J. Passive thermographic detection of moisture problems in façades with adhered ceramic cladding. Constr Build Mater. 2014; doi:10.1016/J.CONBUILDMAT.2013.10.085.

46. Cadelano G, Bison P, Bortolin A, Ferrarini G, Peron F, Girotto M, Volinia M. Monitoring of historical frescoes by timed infrared imaging analysis. Opto- Electronics Review. 2015; doi:10.1515/oere-2015-0012.

47. Georgescu MS, Ochinciuc CV, Georgescu ES, Colda I. Heritage and climate changes in Romania: the St. Nicholas Church of Densus, from degradation to restoration. Energy Procedia. 2017; doi: 10.1016/j.egypro.2017.09. 374.

48. ASTM C1153-10:2010. Standard practice for location of wet insulation in roofing systems using infrared imaging. West Conshohocken: ASTM International; 2010.

49. ASTM C1060-90:2003. Standard practice for thermographic inspection of insulation installations in envelope cavities of frame buildings. West Conshohocken: ASTM International; 2003.

50. Bradski G, Kaehler A. Learning OpenCV. O'Reilly. 2008. https://www.bogotobogo.com/cplusplus/files/OReilly%20Learning%20OpenCV.pdf. Accessed 30 Nov 2018.

51. Hamledari H, McCabe B, Davari S. Automated computer vision-based detection of components of under-construction indoor partitions. Autom Constr. 2017; doi:10.1016/J.AUTCON.2016.11.009.

52. Mordvintsev A, Rahman A. OpenCV-Python Tutorials Documentation. 2017. https://media.readthedocs.org/pdf/opencv-python-tutroals/latest/opencv-python-tutroals.pdf. Accessed 30 Nov 2018.

53. Image Filtering — OpenCV 2.4.13.5 documentation. 2017. https://docs.opencv.org/2.4/modules/imgproc/doc/filtering.html#bilateralfilter. Accessed 30 Nov 2018.

54. 1.3.5.11. Measures of Skewness and Kurtosis. NIST/SEMATECH E-handb. Stat. Methods. 2003. https://www.itl.nist.gov/div898/handbook/eda/section3/eda35b.htm. Accessed 30 Nov 2018.

55. George D, Mallery P. SPSS for Windows Step by Step: A Simple Guide and Reference 17.0 Update. 10th ed. Boston: Pearson; 2010.

56. scipy.stats.skew — SciPy v0.13.0 Reference Guide. https://docs.scipy.org/doc/scipy-0.13.0/reference/generated/scipy.stats.skew.html. Accessed 30 Nov 2018.

57. scipy.stats.kurtosis — SciPy v1.1.0 Reference Guide. https://docs.scipy.org/doc/scipy/reference/generated/scipy.stats.kurtosis.html. Accessed 30 Nov 2018.

58. Xu X, Xu S, Jin L, Song E. Characteristic Analysis of Otsu Threshold and its Applications. Pattern Recognit Lett. 2011; doi:10.1016/j.patrec.2011.01.021.

59. Yuan X, Wu L, Peng Q. An improved Otsu method using the weighted object variance for defect detection. Appl Surf Sci. 2015; doi:10.1016/j.patrec.2011.01.021.

60. OpenCV: Image Thresholding. https://docs.opencv.org/3.4.0/d7/d4d/tutorial_py_thresholding.html. Accessed 30 Nov 2018.